

The electrochemical self-assembly of hierarchical dendritic Bi₂Se₃ nanostructures (Postprint)

Authors: Han, C, Yang, J, Yan, C, Li, Y, Liu, FY, Jiang, LX, Ye, JC, Liu, YX

Date: 2017-04-06T00:00:00+00:00

Abstract

Bismuth selenide (Bi₂Se₃) has proven to be an important material in thermoelectric and topological insulator applications. We report here a simple electrochemical self-assembly route for the preparation of well-defined hierarchical dendritic Bi₂Se₃ nanost

Full Text

Preamble

Cite this: CrystEngComm, 2014, 16, Received 10th October 2013, Accepted 20th December 2013

The electrochemical self-assembly of hierarchical dendritic Bi Se nanostructures

Can Han,^{ab} Jia Yang,^a Chang Yan,^a Yi Li,^a Fangyang Liu,^a *Liangxing Jiang,^a Jichun Yeb* and Yexiang Liu

Bismuth selenide (Bi Se) has proven to be an important material in thermoelectric and topological insulator applications. We report here a simple electrochemical self-assembly route for the preparation of well-defined hierarchical dendritic Bi Se nanostructures. Cyclic voltammetry was used to study the electrochemical reactions relevant to the growth of the prepared bismuth selenide. The compositional, morphological and structural properties of the deposited nanostructures were characterized using energy dispersive X-ray spectroscopy (EDS), scanning electron microscopy (SEM), transmission electron microscopy (TEM), X-ray diffraction (XRD), Raman spectroscopy and X-ray photoelectron spectroscopy (XPS). The band gap of the prepared Bi Se dendritic nanostructures was estimated to be 0.50 ± 0.01 eV by a UV-VIS-NIR spectrophotometer, and the dendritic Bi Se nanostructures showed excellent photoelectrochemical activity. Additionally, based on investigation of the evolution of the morphology and

composition during electrochemical growth, a possible formation mechanism of the dendritic structures was proposed. Furthermore, the effects of some synthesis conditions on the morphologies of the deposited bismuth selenide nanostructures were studied.

1. Introduction

Due to size, dimensionality and grain boundary structure effects, nanostructured materials exhibit peculiar and unique properties superior to those of bulk materials. For example, fundamental electrical and optical properties such as electrical conductivity and band gap can be tuned to desired levels as material dimensions evolve from bulk phases to nanostructures.¹ In recent years, nanoscale materials have found extensive potential applications in thermoelectric and optical devices, electronics, magnetics and catalysis. Nanostructures include nanoparticles, nanorods, nanowires, nanotubes, nanobelts, quantum dots, etc. Building these nano-building blocks into complex three-dimensional hierarchical architectures combines the advantages of these nanoscale constructing units, representing an important approach to realize functional nanosystems that has stimulated great interest.¹

As ubiquitous hierarchical structures in nature that follow branching growth patterns with a main stem and side branches,¹ dendritic materials show potential for many applications. To date, many approaches have been developed for controllable growth of hierarchically dendritic structured materials, including vapor-liquid-solid (VLS),¹ layer-by-layer (LBL),² hydrothermal methods,²¹ electrodeposition²² and others. Among these techniques, electrodeposition presents a simple, rapid and economical method that has been widely applied, especially in functional material preparation.²²

Bismuth selenide (BiSe) is a narrow band-gap semiconductor ($E_g = 0.35$ eV)² that exhibits great potential in thermoelectric² and topological insulator (TI) applications.² In recent years, bismuth selenide compounds have been prepared as thin films or nanostructures, including nanorods, nanospheres, nanowires, nanosheets and nanotubes.²⁻³³ Among various fabrication methods, the electrochemical approach has been considered promising from the viewpoint of simplicity, low cost and feasibility for large-area production.³ Li et al. reported the preparation of BiSe thin films through electrodeposition using Bi(NO₃)₃ and SeO₂ as starting materials.³ Xiao et al. studied the electrochemical behaviors during formation of bismuth selenide thin films via electrochemical atomic layer deposition.³ Torane et al. accomplished preparation of BiSe thin films from both an acidic bath³ and a nonaqueous medium.³ Furthermore, BiSe thin films have also been fabricated by galvanostatic deposition.³ However, there have been no reports to date about preparation of hierarchical nanostructured bismuth selenide compounds via a simple electrochemical process.

In this paper, we report for the first time an electrochemical synthesis of novel hierarchical dendritic nanostructures of bismuth selenide from an electrolyte so-

lution using $\text{Bi}(\text{NO}_3)_3 \cdot 5\text{H}_2\text{O}$ and SeO_2 as ion sources and KSCN as a complexing agent. Based on our experimental results, a possible formation mechanism is proposed. In addition, the effects of synthesis conditions such as KSCN additives in the electrolyte, deposition potential and deposition temperature on the morphology of the bismuth selenide nanostructures are discussed.

2. Experimental

The electrochemical experiments, including cyclic voltammetry (CV) and electrodeposition, were carried out in a stagnant three-electrode cell configuration with a commercial SnO_2 -coated glass substrate (Qinhuangdao Yaohua Xingye Coating Glass Co., Ltd, China, $20 \Omega \text{ cm}^2$) as the working electrode, a pure graphite plate as the counter electrode and a saturated calomel electrode (SCE) as the reference electrode. All potentials in this work were reported with respect to this reference.

The SnO_2 -coated glass substrates were ultrasonically cleaned sequentially in acetone, ammonia and alcohol, then rinsed with deionized water ($18.2 \text{ M}\Omega \text{ cm}^2$) and subsequently dried. The electrolyte solution contained 2 mM $\text{Bi}(\text{NO}_3)_3$, 2.5 mM H_2SeO_4 , and 0–20 mM KSCN as a complexing agent. The pH of the electrolyte was adjusted to 0.50 by adding drops of concentrated HNO_3 .

A Princeton Applied Research 2273A potentiostat was used for all electrochemical experiments. The cyclic voltammograms were measured at a scan rate of 5 mV s^{-1} and scanned first in the negative direction. All film depositions and CV measurements were performed in a stagnant bath to maintain the designed temperature.

The chemical composition of the obtained deposits was characterized by energy dispersive X-ray spectroscopy (EDS, EDAX-GENESIS60S). The morphologies of the bismuth selenide samples were observed using scanning electron microscopy (SEM, Nova Nano SEM230) and transmission electron microscopy (TEM, JEM-2100F), by which the corresponding selected area electron diffraction (SAED) and high-resolution transmission electron microscopy (HRTEM) results were also collected.

In addition, the crystalline phase of the products was identified by X-ray diffraction (XRD, Rigaku 3014). Element identification and valence state analysis were conducted by X-ray photoelectron spectroscopy (XPS, K-Alpha 1063). Raman spectroscopy (Jobin-Yvon LabRAM HR-800, Horiba) was used to further confirm the phase composition of the electrodeposited products. Furthermore, the optical and electrical properties of the deposits were measured by a UV-VIS-NIR spectrophotometer (Hitachi U-4100) and photoelectrochemical (PEC) tests (photocurrent-potential tests). The PEC tests were carried out in a 0.5 M H_2SO_4 solution, and a Newport 300 W xenon lamp was used as the light source with the light intensity kept at 100 mW cm^{-2} .

3.1. Cyclic voltammograms of the unitary Bi and Se systems and the binary Bi-Se system

The electrochemical reactions relevant to the growth of bismuth selenide intermetallic compounds were studied by cyclic voltammetry. Fig. 1a [Figure 1: see original paper] shows the cyclic voltammograms for the SnO electrode in the unitary Bi system containing 2 mM Bi(NO₃)₃ and 10 mM KSCN. It should be noted that cathodic/anodic peak potentials are used in our CV analysis rather than the half-wave potential to simplify the analysis process. From Fig. 1a, two distinct waves with a cathodic peak at about -0.23 V and an anodic peak at about 0.06 V can be observed, corresponding to the reductive deposition of Bi³⁺ in the solution (eqn (1)) and the oxidative dissolution of the deposited Bi, respectively.³² In addition, another cathodic peak appears at about -0.65 V in the curve, which can be attributed to hydrogen evolution in the electrolyte solution (eqn (2)).³

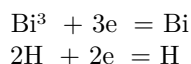


Fig. 1b illustrates the cyclic voltammograms for the SnO electrode in the unitary Se system containing 2.5 mM H₂SeO₄ and 10 mM KSCN. For the H₂SeO₄ solution, the curve displays two cathodic peaks at -0.17 V and -0.61 V. Based on previous studies,¹ the weak cathodic wave with a peak at about -0.17 V corresponds to selenium deposition through the four-electron reduction of Se(IV) to Se(0) as described by eqn (3). Another cathodic wave with a peak at about -0.61 V corresponds to the six-electron reduction of Se(IV) to Se(-II) according to eqn (4). The product Se(-II) then undergoes a comproportionation reaction with Se(IV) in solution (eqn (5)), leading to the chemical formation of Se(0). This process of selenium deposition via reactions (4) and (5) appears similar to the four-electron reduction (eqn (3)) when the concentration of H₂SeO₄ is sufficiently high. Furthermore, the anodic current remains negative with no obvious peak emerging during the positive scanning process, indicating that the applied potentials were not positive enough for oxidation of Se—very little of the deposited selenium was redissolved. This observation is also confirmed by the essentially unchanged color and thickness of the deposits during our experiments.

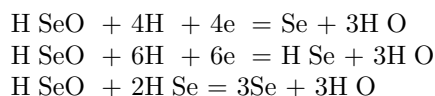
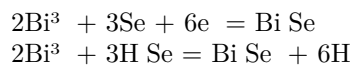


Fig. 1c presents the cyclic voltammograms for the SnO electrode in the binary Bi-Se system containing 2 mM Bi(NO₃)₃, 2.5 mM H₂SeO₄ and 10 mM KSCN. During the negative scanning process of the applied potential, a cathodic wave peaking between -0.05 V and -0.20 V with much larger current density than that of the unitary Se system is observed, which can be ascribed to deposition of Bi₂Se₃. This assignment is supported by subsequent characterization of the deposits and because the reductive deposition of Se occurs earlier than that

of Bi, which then induces formation of Bi Se with Bi³⁺ in solution (eqn (6)), releasing a Gibbs free energy of $-316.392 \text{ kJ mol}^{-1}$ (at 298 K). Compared with the reductive peak of Bi³⁺ at -0.23 V in the unitary Bi system (Fig. 1a), the deposition of Bi Se shows a significant positive shift. This characteristic indicates an induced underpotential deposition mechanism caused by the large free energy release during Bi Se formation. In addition, the peak corresponding to the six-electron reduction reaction of Se also shows an obvious positive shift, suggesting that this Bi Se-modified surface lowers the overpotential for H SeO reduction; the generated H Se immediately reacts with Bi³⁺ in solution according to eqn (7). Thus, the other cathodic wave with a peak at about -0.43 V (Fig. 1c) can be reasonably assigned to another route of Bi Se formation via reaction (7). Regarding the anodic wave, the continuous negative anodic current shows that the applied potentials were not positive enough for oxidation of the deposits, while peaks at about 0.02 V and 0.35 V may correspond to the inconspicuous oxidation of Bi and Bi Se, respectively.^{32, 2}



3.2. The characterization of the prepared Bi Se nanostructures

A typical potentiostatic electrolysis of bismuth selenide compound films was carried out at -0.15 V in a solution containing $2 \text{ mM Bi(NO}_3)_3$, 2.5 mM H SeO_4 and 10 mM KSCN for 60 min at room temperature ($25 \text{ }^\circ\text{C}$). The surface morphologies of the deposits were examined by SEM, and representative images at different magnifications are shown in Fig. 2 [Figure 2: see original paper]. Fig. 2a clearly shows that the prepared sample has a symmetrical dendritic shape with spiked branches. The central trunk is composed of orderly, close-packed secondary branches hundreds of nanometers in size, and the total length of the prepared bismuth selenide dendrites can reach $5\text{--}10 \text{ }\mu\text{m}$. The higher magnification SEM image in Fig. 2b reveals that these secondary branches are actually constructed from orderly nanoparticles several nanometers in size (circled in the figure). The representative EDS pattern of the deposits is shown in Fig. 3 [Figure 3: see original paper], where selenium peaks at about 1.25 keV and 11.25 keV and bismuth signals at about 2.50 keV and 10.75 keV are observed. Composition analysis revealed 39.88 atom\% Bi and 60.12 atom\% Se , implying the stoichiometry of Bi Se for the prepared deposits.

Fig. 4 [Figure 4: see original paper] shows the typical XRD pattern of the electrodeposited bismuth selenide compounds, which is consistent with a rhombohedral Bi Se crystal structure [space group (R3m) (166)]. The unit cell of Bi Se can be displayed using a hexagonal coordinate system (JCPDS 33-0214). For this crystalline structure, layered Bi Se is composed of hexagonal close-packed atomic layers periodically arranged along the c-axis with quintuple layers ordered in the Se-Bi-Se-Bi-Se sequence,³ as shown in the inset of Fig. 4. Additionally, SnO peaks from the substrate are also observed.

Further characterization by transmission electron microscopy (TEM) was performed. The TEM image of the prepared Bi Se dendrite is shown in Fig. 5a [Figure 5: see original paper], and the corresponding typical SAED pattern recorded from the top of the central trunk is presented in the inset. The electron diffraction pattern consists of diffraction spots and polycrystalline rings, indicating that the dendritic Bi Se nanostructures are polycrystalline. The brightest diffraction spots in the SAED pattern correspond to the (0 1 5) crystal plane, consistent with the main diffraction peak in the previous XRD pattern. Further analysis was conducted via a typical HRTEM image recorded at the fringe of a branch (Fig. 5b). A series of parallel alternating dark and bright stripes is visible, though the crystal orientation of each grain differs. Spacings of 2.24 nm and 2.11 nm correspond to the (1 0 10) and (0 1 11) planes, respectively. The angle between these two faces is 63.4° , also in good agreement with lattice parameters for hexagonal Bi Se (JCPDS card no. 33-0214). Fig. 5c shows the Fourier transform (FFT) pattern of Fig. 5b, with crystal planes corresponding to different bright spots marked.

Surface analysis of the prepared bismuth selenide sample was carried out using X-ray photoelectron spectroscopy (XPS), which is widely applied for element identification, valence state determination and semi-quantitative estimation in compounds. Fig. 6 [Figure 6: see original paper] shows the XPS spectra of the as-prepared Bi Se nanostructures. The survey spectrum (Fig. 6a) reveals no peaks for elements other than Bi, Se, O, C and Sn, indicating high purity of the product.² High-resolution core spectra for Se 3d and Bi 4f are shown in Fig. 6b and c. The Se 3d spectrum consists of two peaks related to the valence state of Se(-II) in Bi Se compounds: one at about 53.45 eV corresponding to Se 3d / and another at 54.18 eV corresponding to Se 3d / . These binding energies show a splitting of 0.73 eV (vs. reported value of 0.7 eV). For the Bi 4f spectrum, the Bi 4f / peak at about 157.98 eV and the 4f / peak at about 164.28 eV related to the valence state of Bi(III) in Bi Se compounds are observed in Fig. 6c, displaying a splitting of 5.30 eV (matching reported values). Furthermore, comparing these data with those of pure bulk elemental Se and Bi reveals a red shift of about 1.1 eV for Se and a blue shift of about 1.38 eV for Bi. These opposite shifts are caused by charge transfer from Bi to Se when chemical bonds form in the bismuth selenide compound. Related data are presented in Table 1 , which agree well with information reported for Bi³ and Se² in Bi Se compounds.³ However, two additional peaks corresponding to Bi 4f in Bi O were detected, with Bi 4f / at about 159.08 eV and 4f / at about 164.38 eV, suggesting that some Bi atoms on the sample surface were oxidized in air.

To further confirm phase information, Raman spectroscopy was used to characterize the prepared Bi Se nanostructures, with the corresponding spectrum shown in Fig. 7 [Figure 7: see original paper]. Three characteristic peaks appear at 69 cm^{-1} , 129 cm^{-1} and 171 cm^{-1} , respectively consistent with the three vibrational modes A g², Eg and A g¹ reported for the Bi Se phase.³ Additionally, a peak corresponding to Bi O at 94 cm^{-1} (ref. 48) was observed, implying partial oxidation of Bi in the deposits, which accords with XPS results.

To preliminarily estimate the performance of the synthesized dendritic nanostructures compared with Bi₂Se₃ film (prepared at -0.15 V and 50 °C in an electrolyte solution containing 2 mM Bi(NO₃)₃, 2.5 mM H₂SeO₄ and 10 mM KSCN), optical transmittance tests using a UV-VIS-NIR spectrophotometer and photoelectrochemical tests were conducted. According to optical transmittance tests, the absorption coefficients of both samples exceed 10 cm⁻¹ in the visible region (about 350 – 770 nm), supporting the direct band gap nature of the material. Fig. 8 [Figure 8: see original paper] shows plots of $(\alpha h\nu)^2$ versus $h\nu$ (photon energy), converted from transmission spectra recorded in the wavelength range of 300 – 2500 nm without accounting for reflection and scattering losses. Based on allowed direct interband transition, the band gaps of the Bi₂Se₃ nanostructured dendrites and Bi₂Se₃ film are determined to be 0.50 ± 0.01 eV and 0.35 ± 0.01 eV, respectively. The estimated value for the Bi₂Se₃ dendritic nanostructures is higher than the reported 0.35 eV² for common Bi₂Se₃ thin films, which can be reasonably ascribed to energy level separation as crystallite size decreases.¹

Fig. 9 [Figure 9: see original paper] displays photocurrent–potential curves obtained from photoelectrochemical tests of both deposited dendritic Bi₂Se₃ nanostructures and Bi₂Se₃ film in 0.5 M H₂SO₄ solution. The onset potential of photocurrent occurs at about 0.3 V, and photocurrent densities increase with negative shift of the cathodic potential, indicating p-type conductivity for both samples.² Nevertheless, photocurrent densities of the Bi₂Se₃ nanostructures are visibly higher than those of the Bi₂Se₃ film, demonstrating that the obtained dendritic Bi₂Se₃ nanostructures possess better photoelectrochemical properties than the Bi₂Se₃ film. This phenomenon can be attributed to the large specific surface area of the dendritic nanostructures, which provides adequate region for separation of electron-hole pairs at the semiconductor/solution interface. Moreover, the photocurrent–potential curve of the Bi₂Se₃ film shows obvious electrochemical reductive peaks as the applied potential scans negatively, while the curve for the dendritic Bi₂Se₃ nanostructures presents a much more stable variation pattern, indicating that the dendritic Bi₂Se₃ nanostructures have purer phase construction and more stable photochemical response than the Bi₂Se₃ film.³ All these results confirm that dendritic Bi₂Se₃ nanostructures were obtained in this work. To our knowledge, this is the first report that hierarchical dendritic Bi₂Se₃ nanostructures can be prepared via electrodeposition. Furthermore, the prepared dendritic Bi₂Se₃ nanostructures show excellent photoelectrochemical activity.

3.3. The possible growth mechanism of the dendritic Bi₂Se₃ nanostructures and the effects of the additive, deposition potential and temperature on morphology and composition

To clarify the formation mechanism of the dendritic structure, the evolution of morphology with time extension was investigated as shown in Fig. 10a [Figure 10: see original paper]–e. At the initial electrodeposition stage (Fig. 10a), clusters developed from electrochemical nucleation and growth with a mean size of

about 500 nm formed dispersedly on the substrate, some of which began growing in preferred orientations, showing an original dendritic shape (inset of Fig. 10a). When deposition time was extended to 5 min, the clusters became dense and distributed homogeneously across the substrate (Fig. 10b). As deposition continued, almost all clusters developed into hierarchical dendritic structures (Fig. 10c), which showed further increased volume (Fig. 10d) and sub-branches (inset of Fig. 10d). Notably, significant differentiation in volume appeared between these hierarchical dendritic structures during electrochemical nonequilibrium growth, as seen in Fig. 10e. Larger dendrites could capture reactive ions from the bulk electrolyte more easily, leading to further size increase of their trunks and branches, eventually covering the whole substrate as displayed in Fig. 10f. Smaller clusters appeared to stop growing due to lack of reactive species nearby, as identified in the circle of Fig. 10f.

Atomic compositions of deposits at different durations were obtained using EDS, as shown in Fig. 11 [Figure 11: see original paper]. A noticeable phenomenon is that when deposition time was less than 10 minutes, the average atom ratios of Bi and Se across the specimens showed an increasing trend until reaching the 2:3 ratio, while the composition detected at dendritic structure locations (inset of Fig. 11) had Bi Se stoichiometry from the very beginning and maintained this ratio as deposition proceeded. In other words, the Bi Se dendritic nanostructures were self-assembled from Se-rich deposits formed in the initial electrodeposition stage. Combined with previous CV curves of unitary Bi and Se systems (Fig. 1a and b), the potential corresponding to the reductive peak of H SeO is more positive than that of Bi³⁺ ions in the electrolyte, thus Se deposition occurred earlier than Bi deposition. We propose that at the beginning of deposition, Se ions were deposited first, which then induced reduction of Bi ions in the electrolyte. It is noteworthy that besides some deposited Se participating in assembly of Bi Se compound clusters, redundant Se resulted in higher Se content across the specimen than at cluster locations. As deposition continued, Bi³⁺ ions with increased concentration in the electrolyte were reduced to combine with deposited Se, forming more Bi Se compounds that grew along preferred directions, sprouting branches and sub-branches sequentially. Finally, well-defined hierarchical dendritic Bi Se nanostructures were fabricated.

Based on the above analysis, the evolution process of the obtained Bi Se dendritic nanostructures should follow these rules: first, clusters with Bi Se stoichiometry form from a Se-rich environment, which subsequently develop into a primitive dendritic shape at the early stage; then, branches and sub-branches develop from the original dendrites, eventually growing into hierarchical nanostructures.

In our experiments, KSCN concentration was found to be a key factor affecting the morphologies of prepared bismuth selenides. Fig. 12a [Figure 12: see original paper]-e illustrates morphology changes with varying KSCN concentration. Without KSCN, thin films with flower-like clusters composed of wispy nanosheets were obtained (Fig. 12a). With 5 mM KSCN, bismuth selenide

compounds formed lumps with different shape control (Fig. 12b). When KSCN concentration reached 10 mM, morphology changed to the desired dendritic nanostructures (Fig. 12c). With 15 mM KSCN addition, dendritic structures grew thicker (Fig. 12d), and a dramatic morphological transition from dendritic to flower-like occurred when 20 mM KSCN was added (Fig. 12e). The remarkable impact of KSCN on producing Bi Se with dendritic nanostructured morphology can be reasonably attributed to the adsorption effect of KSCN. KSCN is a common chemical reagent in the electroplating industry, containing a thiocyanate group that acts as a ligand in the electrolyte. According to the Gibbs-Wulff theorem, additives can control sample morphology by tuning surface energies of specific crystallographic faces. Generally, when inorganic crystals form under equilibrium conditions, the growth direction is determined by the relative order of surface energies. During electrodeposition, when an appropriate amount of KSCN is introduced into the electrolyte, Bi^{3+} and SeO_4^{2-} ions near the crystal surface are likely reduced, and deposited atoms adsorb on some positive polar faces without additive passivation, resulting in faster growth along certain directions (such as the (0 1 5) plane in this study). However, when no or little KSCN is added, deposited bismuth selenides grow basically according to their intrinsic crystal surface energy, as shown in Fig. 12a and b. Conversely, deposits from electrolytes with excessively high KSCN concentration also grow in uncertain orientations due to excess passivation effects on various crystal planes, as observed in the flower-like morphology of Fig. 12e.

Furthermore, as important parameters in electrodeposition technology, the effects of deposition potential and temperature were also investigated. Fig. 13 [Figure 13: see original paper] presents morphology and dimension changes caused by deposition potential. At -0.05 V, the product consisted of clusters with nanosheets (Fig. 13a), and a dramatic morphology change occurred when deposition potential reached -0.10 V. As seen in Fig. 13b, immature dendritic structures were obtained at this potential. When deposition potential was -0.15 V and -0.20 V, the dendrites developed into well-defined hierarchical dendritic nanostructures. However, as deposition potential reached -0.25 V, deterioration in dendritic morphology emerged, and homogeneity of hierarchical dendritic structures on the substrate became markedly weakened. Additionally, EDS analysis of deposits in Fig. 14 [Figure 14: see original paper] shows that the composition of deposited bismuth selenides maintains Bi Se stoichiometry with changing deposition potential, illustrating that the electrochemical process of bismuth selenides follows a diffusion-controlled pathway, providing essential conditions for promoting formation of the desired hierarchical dendritic nanostructured products.

Fig. 15 [Figure 15: see original paper] shows morphology evolution with changing deposition temperature. Dendritic structures gradually degenerate as deposition temperature increases. This phenomenon should be ascribed to the elimination effect of temperature increase on ion concentration polarization in the electrolyte, which is the governing factor in diffusion-controlled processes.

4. Conclusions

Well-defined hierarchical dendritic Bi₂Se₃ nanostructures have been synthesized on SnO₂-coated glass substrates by potentiostatic electrodeposition from an aqueous acid bath containing Bi(NO₃)₃, H₂SeO₄ and KSCN at 25 °C. The dendritic Bi₂Se₃ nanostructures have a band gap of 0.50 ± 0.01 eV and show more excellent photoelectrochemical properties than Bi₂Se₃ film. Combined with CV analysis and experimental results, the hierarchical Bi₂Se₃ dendritic nanostructures grow from primitive dendrites, which develop from clusters formed in a Se-rich environment at the initial electrodeposition stage. Furthermore, KSCN was found to be a structure-directing agent that affects product morphology. In addition, deposition potential and temperature also play important roles in determining the morphologies of prepared bismuth selenides.

Acknowledgements

This work is supported by the National High Technology Research and Development Program of China (863 Program, grant no. 2012AA050703) and the National Natural Science Foundation of China (grant nos. 51222403 and 51204214).

References

1. P. Gupta, R. Pal, D. Bhattacharyya, S. Chaudhuri and A. K. Pal, *Phys. Status Solidi A*, 1995, 148, 459-467.
2. B. Poudel, Q. Hao, Y. Ma, Y. Lan, A. Minnich, B. Yu, X. Yan, D. Wang, A. Muto, D. Vashaee, X. Chen, J. Liu, M. S. Dresselhaus, G. Chen and Z. Ren, *Science*, 2008, 320, 634-638.
3. G.-R. Li, Q.-F. Ke, G.-K. Liu, P. Liu and Y.-X. Tong, *Mater. Lett.*, 2007, 61, 884-888.
4. G.-R. Li, F.-L. Zheng and Y.-X. Tong, *Cryst. Growth Des.*, 2008, 8, 1226-1232.
5. B. R. Sankapal, R. S. Mane and C. D. Lokhande, *Mater. Chem. Phys.*, 2000, 63, 230-234.
6. Z. Sun, S. Liufu, X. Chen and L. Chen, *CrystEngComm*, 2010, 12, 2672-2674.
7. X. Qiu, L. N. Austin, P. A. Muscarella, J. S. Dyck and C. Burda, *Angew. Chem., Int. Ed.*, 2006, 45, 5656-5659.
8. M.-X. Wang, C. Liu, J.-P. Xu, F. Yang, L. Miao, M.-Y. Yao, C. L. Gao, C. Shen, X. Ma, X. Chen, Z.-A. Xu, Y. Liu, S.-C. Zhang, D. Qian, J.-F. Jia and Q.-K. Xue, *Science*, 2012, 336, 52-55.
9. L. Alegria, M. Schroer, A. Chatterjee, G. Poirier, M. Pretko, S. Patel and J. Petta, *Nano Lett.*, 2012, 12, 4711-4714.
10. G. Zhang, H. Qin, J. Teng, J. Guo, Q. Guo, X. Dai, Z. Fang and K. Wu, *Appl. Phys. Lett.*, 2009, 95, 1-3.
11. S. Xu, W.-B. Zhao, J.-M. Hong, J.-J. Zhu and H.-Y. Chen, *Mater. Lett.*,

- 2005, 59, 319-321.
12. H. Peng, J. Zhou, D. Tang, Y. Lai, F. Liu, J. Li and Y. Liu, *Chem. Commun.*, 2012, 48, 2603-2605.
 13. H. Peng, K. Lai, D. Kong, S. Meister, Y. Chen, X.-L. Qi, S.-C. Zhang, Z.-X. Shen and Y. Cui, *Nat. Mater.*, 2010, 9, 225-229.
 14. H. Cui, H. Liu, X. Li, J. Wang, F. Han, X. Zhang and R. Boughton, *J. Solid State Chem.*, 2004, 177, 4001-4006.
 15. A. P. Torane, C. D. Lokhande, P. S. Patil and C. H. Bhosale, *Scr. Mater.*, 2012, 67, 249-252.
 16. X.-L. Li, K.-F. Cai, H. Li, L. Wang and C.-W. Zhou, *Int. J. Miner., Metall. Mater.*, 2010, 17, 104-107.
 17. G.-R. Li, C.-Z. Yao, X.-H. Lu, F.-L. Zheng, Z.-P. Feng, X.-L. Yu, C.-Y. Su and Y.-X. Tong, *Chem. Mater.*, 2008, 20, 3306-3314.
 18. C. Zhu, G. Meng, Q. Huang, Z. Huang and Z. Chu, *Cryst. Growth Des.*, 2011, 11, 748-752.
 19. H. Liang, Z. Li, W. Wang, Y. Wu and H. Xu, *Adv. Mater.*, 2009, 21, 4614-4618.
 20. D. P. Serrano, J. Aguado, M. José, J. M. Rodríguez and Á. Peral, *Chem. Mater.*, 2006, 18, 2462-2464.
 21. Y. J. Song, J. Y. Kim and K. W. Park, *Cryst. Growth Des.*, 2008, 9, 505-507.
 22. G.-R. Li, F.-L. Zheng and Y.-X. Tong, *Cryst. Growth Des.*, 2008, 8, 1226-1232.
 23. M. Kimura, Y. Sugihara, T. Muto, K. Hanabusa, H. Shirai and N. Kobayashi, *Chem.-Eur. J.*, 1999, 5, 3495-3500.
 24. M. O. Orlandi, E. R. Leite, R. Aguiar, J. Bettini and E. Longo, *J. Phys. Chem. B*, 2006, 110, 6621-6625.
 25. G. Wang, Y. Fang, P. Kim, A. Hayek, M. R. Weatherspoon, J. W. Perry, K. H. Sandhage, S. R. Marder and S. C. Jones, *Adv. Funct. Mater.*, 2009, 19, 2768-2776.
 26. Y. Wang, G. Xu, L. Yang, Z. Ren, X. Wei, W. Weng, P. Du, G. Shen and G. Han, *J. Cryst. Growth*, 2009, 311, 2519-2523.
 27. G.-R. Li, X.-H. Lu, D.-L. Qu, C.-Z. Yao, F.-L. Zheng, Q. Bu, C.-R. Dawa and Y.-X. Tong, *J. Phys. Chem. C*, 2007, 111, 6678-6683.
 28. S. Ham, S. Jeon, M. Park, S. Choi, K.-J. Paeng, N. Myung and K. Rajeshwar, *J. Electroanal. Chem.*, 2010, 638, 195-203.
 29. H. Peng, K. Lai, D. Kong, S. Meister, Y. Chen, X.-L. Qi, S.-C. Zhang, Z.-X. Shen and Y. Cui, *Nat. Mater.*, 2010, 9, 225-229.
 30. W. Richter, H. Köhler and C. R. Becker, *Phys. Status Solidi B*, 1977, 84, 619-628.
 31. V. B. Nascimento, V. E. de Carvalho, R. Paniago, E. A. Soares, L. O. Ladeira and H. D. Pfannes, *J. Electron Spectrosc. Relat. Phenom.*, 1999, 104, 99-107.
 32. R. Li, W. Chen, H. Kobayashi and C. Ma, *Green Chemistry*, 2010, Supplementary Material (ESI).
 33. A. J. Salazar-Pérez, M. A. Camacho-López, R. A. Morales-Luckie and V.

- Sánchez-Mendieta, *Superficies Vacío*, 2005, 18, 4-8.
34. S. M. Pawar, A. V. Moholkar, U. B. Suryavanshi, K. Y. Rajpure and C. H. Bhosale, *Sol. Energy Mater. Sol. Cells*, 2007, 91, 714-720.
 35. S. A. Gamboa, P. J. Sebastian, X. Mathew, H. Nguyen-Cong and P. Chartier, *Sol. Energy Mater. Sol. Cells*, 1999, 59, 115-123.
 36. C. J. Huang, T. H. Meen, M. Y. Lai and W. R. Chen, *Sol. Energy Mater. Sol. Cells*, 2004, 82, 553-565.
 37. J. Yang, F. Liu, Y. Lai, J. Li and Y. Liu, *Electrochem. Solid-State Lett.*, 2012, 15, D19-D21.
 38. H. Cao, X. Qian, C. Wang, X. Ma, J. Yin and Z. Zhu, *J. Am. Chem. Soc.*, 2005, 127, 16024-16025.
 39. J. Xue, W. Liang, X. Liu, Q. Shen and B. Xu, *CrystEngComm*, 2012, 14, 8017-8022.

Note: Figure translations are in progress. See original paper for figures.

Source: ChinaXiv –Machine translation. Verify with original.